Jinst

Published by IOP Publishing for Sissa Medialab

Received: *February 16, 2024*
Revised: *March 20, 2024*
Accepted: *May 16, 2024*
Published: *June 4, 2024*

68th ICFA Advanced Beam Dynamics Workshop on High-Intensity and High-Brightness Hadron Beams — HB2023

Performance of the CERN Proton Synchrotron internal dump: numerical simulation studies and comparison with beam measurements

S. Niang,[a] T. Pugnat,[a] D. Domange,[b] L. S. Esposito,[a] M. Giovannozzi,[a,*] E. Gnacadja,[b] C. Hernalsteens,[a] A. Huschauer[a] and R. Tesse[b]

[a] *CERN,*
Esplanade des Particules 1, 1121 Meyrin, Switzerland
[b] *Université libre de Bruxelles,*
Av. Franklin Roosevelt 50, 1050 Brussels, Belgium

E-mail: massimo.giovannozzi@cern.ch

Abstract: In the framework of the LHC Injector Upgrade project, a new internal dump for the CERN Proton Synchrotron (PS) ring has been designed, installed, and successfully commissioned. This device is designed to move rapidly into the beam and stop charged particles over several thousand turns to provide protection to PS hardware against beam-induced damage. Due to its design, the internal dump absorbs only a fraction of the secondary particles shower produced by the beam particles that impinge on it. The performance of the dump should ensure efficient use throughout the PS energy range, i.e. from injection at 2 GeV (kinetic energy) to flat top at 26 GeV (total energy). This paper presents comprehensive numerical simulations that combine advanced beam dynamics and beam-matter interaction codes to analyse the behaviour of stopped or scattered particles. Based on the impacts computed by multi-turn beam dynamics simulations, detailed shower simulations with FLUKA were performed to assess the impact of the radiation field on downstream equipment, with a particular emphasis on the dose measured by Beam Loss Monitors. The results of these numerical simulations are compared with the data collected during the routine operation of the PS and its internal dump.

Keywords: Accelerator modelling and simulations (multi-particle dynamics, single-particle dynamics); Accelerator Subsystems and Technologies; Beam dynamics

*Corresponding author.

https://doi.org/10.1088/1748-0221/19/06/T06002

2024 JINST 19 T06002

Contents

1 Introduction

During the second long shutdown of the CERN accelerator complex that took place from 2019 to 2021, the internal dumps of the CERN Proton Synchrotron (PS) ring, installed in straight sections (SS) 47 and 48, have been replaced. This was part of the LHC Injector Upgrade (LIU) [1, 2] project. In fact, the goal of this project was an increase in beam brightness to meet the requirements of the LHC luminosity upgrade project (HL-LHC) [3], and this imposed a complete redesign and replacement of the moving dumps installed in the PS ring. The design of the beam dumps involved several steps, starting with a thorough understanding of operational requirements, considering factors such as beam characteristics, achievable movement speed of the dump actuator, and reliability. Simulation and modelling played a crucial role in the design phase, using simplified PS beam dynamics models to account for multiturn effects occurring in the beam-dump interaction and FLUKA [4–6] simulations to assess beam shaving behaviour and particle interactions in the dump core [7]. Detailed thermomechanical numerical simulations using ANSYS® were performed, based on energy deposition maps, through multiple design versions to optimise the dump core material, the cooling system and the actuator mechanism. This iterative process guided the design optimisation, including material selection for the core of the dump (such as graphite and the CuCr1Zr alloy, which offer suitable radiation resistance and mechanical properties) and the implementation of efficient cooling systems using water circuits for the core in ultra-high vacuum [8]. The validation through prototyping ensured that the proposed design met the expectations prior to installation in the PS ring [9].

It should be further noted that the study of beam losses as a function of time and location along the ring resulting from the beam interaction with a moving internal dump represents a novelty for

2024 JINST 19 T06002

the PS accelerator. Studies of losses along the PS ring were carried out for the Continuous Transfer extraction mode, which was used to deliver the beam to the CERN Super Proton Synchrotron over five turns, were carried out in the past [10] but the overall context was different from what is presented here and also less challenging in terms of simulation tools.

The goal of this paper is to further develop the studies carried out during the design phase of the hardware of the PS internal dumps by using the state-of-the-art software that allows simulating both the multiturn dynamics of the proton beams and the complex beam-matter interaction occurring in the internal dumps. Note that an additional complication for numerical simulations is the movement of the dump over the beam revolutions, which requires special tools to be correctly modelled. The novel tools enable us to study in detail the distribution of beam losses along the ring circumference to assess whether additional shielding might be needed to protect the accelerator hardware. The ultimate goal discussed in this paper is to compare the results of numerical simulations with beam-based measurements.

2 Model of the PS ring

The studies presented in this paper are very complex, as they aim to reproduce the behaviour of a beam over several thousands of turns under the effect of the external magnetic fields and the interaction with a moving object, namely the internal dump. Thus, an accurate representation of the beam dynamics and aperture model along the PS ring is required, as well as the beam-matter interactions occurring in the internal dump. Furthermore, the dynamic change of the dump position must be implemented with care.

This section reviews the PS ring layout and the aperture model, presents the different beams and optical configurations used, and finally discusses the mechanical model of the internal dump developed for this study.

2.1 Overview of the PS ring, beam parameters and optical configurations

The Proton Synchrotron (PS) plays a key role in the CERN accelerator complex as it accelerates beams for use at its experimental area, or for fixed-target physics at the Super Proton Synchrotron (SPS), or for collider physics at the Large Hadron Collider (LHC). Its versatility includes the ability to accelerate several particle species (protons and heavy ions), as well as a variety of beam intensities, extraction energies, and highly sophisticated beam manipulations, such as longitudinal beam splitting for the generation of proton beams for the LHC (see, e.g. ref. [11] and references therein) or transverse beam splitting for the Multi-Turn Extraction (MTE) (see, e.g. ref. [12] and references therein).

The PS ring comprises a hundred main magnet units that generate a dipole field with a superimposed quadrupolar field. Each magnet unit is made of two half-units with opposite polarity of the quadrupolar field. The PS lattice has a ten-fold superperiodicity, and in each superperiod a long straight section (SS) accommodates a main RF cavity (see, e.g. refs. [13–17] or ref. [11] for more details on the PS accelerator). Special coils have been added to the main magnets to provide the possibility of controlling the tune and chromaticities, the so-called pole-face windings and the figure-of-eight loop [11]. The effect of these special devices is included in the numerical simulations by means of zero-length multipoles that enable reproducing the measured values of the tune and chromaticities.

Our investigations on the performance of the internal dumps of the PS ring focused on the case of the LHC proton beam and the proton beam for fixed target physics at the SPS. The first beam is a high-brightness beam, extracted at the maximum beam momentum possible, namely 26 GeV/c. The

2024 JINST 19 T06002

second is a high intensity beam, extracted at an intermediate beam momentum of 14 GeV/c. The main parameters of these beams are collected in table 1. Note that the ring tune and chromaticity are adapted to the beam produced.

Table 1. Typical beam and optics parameters used in the numerical simulations for the PS internal dump, which are taken from the specifications [18, 19]. The emittance values represent the normalised rms beam emittances; Q_x, Q_y are the horizontal and vertical tunes, respectively; Q'_x, Q'_y are the horizontal and vertical chromaticities, respectively; $\sigma_\delta, \sigma_\zeta$ represent the rms relative beam momentum spread and rms bunch length, respectively. Note that "LHC" refers to the proton beam used for physics in the LHC, a high-brightness proton beam with a typical bunch intensity of $\approx 1.3 \times 10^{11}$ protons. "SFTPRO" refers to the proton beam for the fixed-target programme at the SPS ring, a high-intensity proton beam with a typical total intensity of $\approx 3 \times 10^{13}$ protons. "FT" stands for the flat-top configuration, corresponding to the extraction energy. "FI" refers to an intermediary magnetic plateau.

		LHC FT	**SFTPRO FT**	**LHC FI**
P	[GeV/c]	26	14	3.9
$\epsilon^*_x/\epsilon^*_y$	[µm]	2.3/2.3	9.0/5.0	2.1/2.1
Q_x		6.217	6.247	6.210
Q_y		6.280	6.298	6.245
Q'_x		≈ 1.7	≈ 3.9	≈ 0.7
Q'_y		≈ 0.4	≈ 1.9	≈ -2.9
σ_δ	[10^{-3}]	0.4	0.1	1.0
σ_ζ	[m]	1.87	9.84	7.50

For an accurate comparison between numerical simulations and beam measurements, not only the optical configurations, but also the closed orbit need to be carefully reproduced. The set of orbit correctors installed in the PS lattice is not suitable for the correction of the closed orbit at high energy. Hence, non-negligible deviations from a zero closed orbit are to be expected for the beams under consideration. Information on the typical value of the measured closed orbit is reported in figure 1, where the markers represent the average of approximately thirty measurements of the closed orbit, with the error bars indicating the rms of the spread between the various measurements. It should be noted that some outliers have been rejected from the analysis. Note that while the closed orbit in the vertical plane is significantly the same for the three PS ring configurations, a sizeable difference is observed in the horizontal plane. In the horizontal plane, the closed orbit distortion show a significant growth with the beam energy, with values rather constant up to beam momentum of 14 GeV/c, and then a sizeable increase is visible, likely due to saturation effects of magnets.

The measured closed orbit has been reproduced in the numerical model of the PS ring by using a set of hundred virtual orbit correctors for each plane located at the junction between the half-units of each main magnet. The results of the fit procedure performed with the `MAD-X` code [20] are also shown in figure 1, where the lines represent the reconstructed closed orbit. A very good agreement is clearly visible.

2.2 Aperture model

The original layout of the mechanical aperture of the PS ring was rather simple [13–17], since the nominal cross section of the vacuum pipe is represented by a quasi-elliptical shape with horizontal

2024 JINST 19 T06002

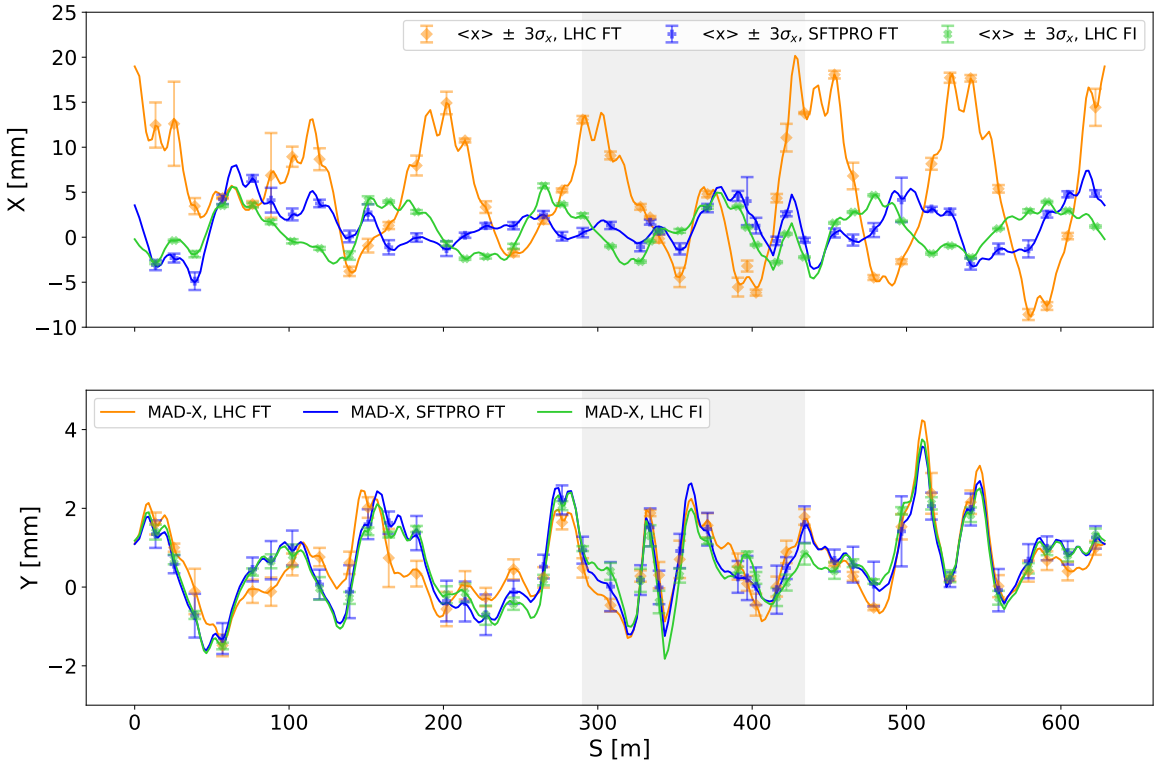

Figure 1. Average of the measured closed orbit (markers) and closed orbit reconstructed with `MAD-X` (lines) that is used in the numerical simulations. The error bars indicate the rms of the spread between the various measurements. The shaded area corresponds to the PS ring region where the beam losses induced by the internal dump occur.

and vertical half axes of 73 mm and 35 mm, respectively. This type of cross section was installed throughout the circumference of the PS ring. With the upgrade of the PS capabilities, and in particular with the implementation of several different extraction types, fast or slow extraction, beam destination, i.e. the machine towards which the extracted beam was delivered, and injection points, for the various types of particles, the mechanical aperture has been upgraded. Practically, this implied the installation of pipes with special cross sections, typically enlarged with respect to the nominal vacuum pipe to ensure enough beam aperture and hence minimise beam losses during operations. The last time the mechanical aperture was reviewed again occurred around 2006, during the implementation of Multi-Turn Extraction (MTE) [12].

All in all, the historical evolution of the mechanical aperture of the PS ring, the way the information is stored in drawings, the features of the cross sections, not always in line with the capabilities of the simulation codes, have made the preparation of a detailed and up-to-date aperture model for the numerical simulations a challenge on its own.

A preliminary numerical simulation campaign had shown that most of the losses generated by the beam-dump interaction occur approximately 120 m downstream of the dump location. Therefore, it was decided to use an elliptical cross section of standard dimensions for most of the circumference of the ring and refine the description of the cross section of the beam pipe only in the region downstream of the two internal dumps, where losses occur, and the aperture variation implemented is shown in figure 2.

2024 JINST 19 T06002

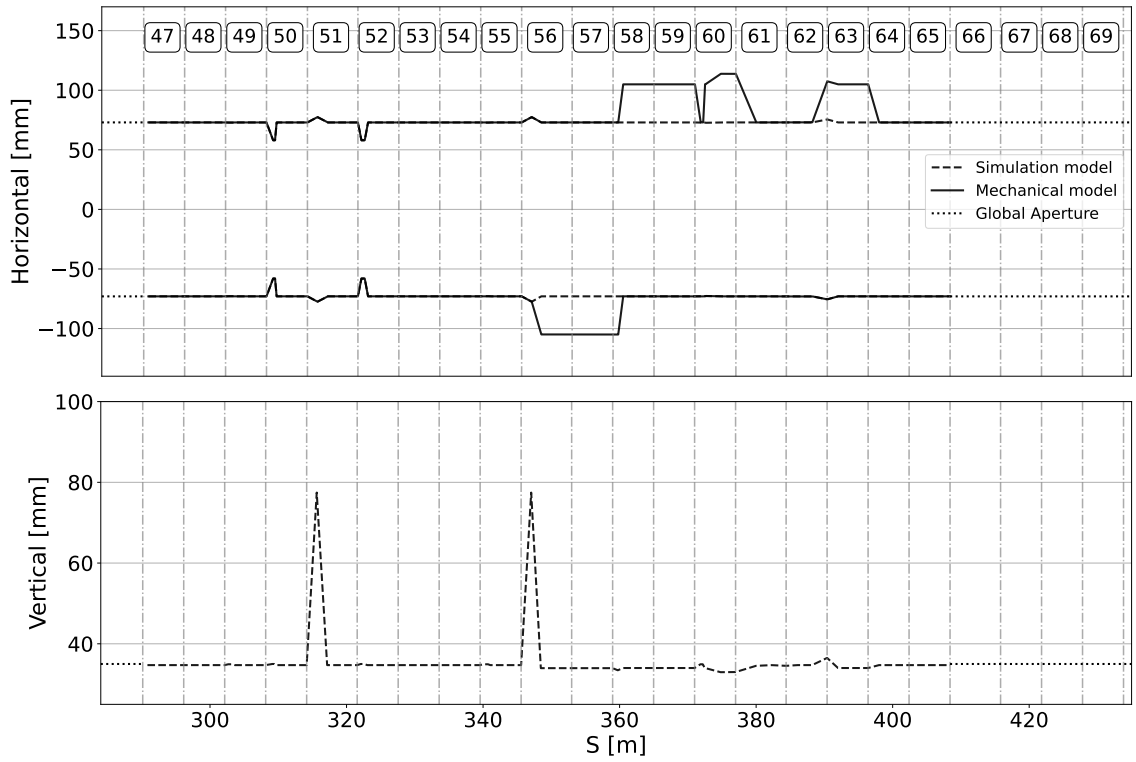

Figure 2. Evolution of the horizontal (top) and vertical (bottom) dimensions of the beam pipe and of the approximation used in the numerical simulations as a function of the distance along the PS circumference. The reference is given by the beginning of SS0 (not shown in the plot, which displays only the region of the PS ring in which the beam losses due to the interaction with the internal dump are distributed). The numbers in the upper part of the top plot stand for the straight section number. Note that while the horizontal aperture is sometimes asymmetric (due to the presence of extraction bumps) the vertical aperture is always symmetric around zero, and for this reason a single curve is plotted.

The horizontal dimension (top) and the half-axis of the vertical dimension (bottom) is shown as a function of the distance from the beginning of the SS0 measured along the circumference of the PS. The numbers in the upper part of the top plot represent the identification number of the straight section and give an indication of the location of the straight section. It is worth stressing that, while the horizontal dimension is not always symmetric around zero, the vertical dimension is, and for this reason a single line is shown. The behaviour in the horizontal plane is due to the presence of injection and extraction bumps, activated only during the injection or extraction processes, to displace the beam to the outside or the inside of the ring, therefore requiring a protrusion of the cross section in the corresponding direction to optimise the available beam aperture. Given the particular application discussed in this paper, in which a circulating beam is considered, with no active orbit bumps, a simplified aperture model has been implemented in which the horizontal vacuum pipe is always symmetric around zero (dashed line in the plots). Note that a Python-based software tool has been developed to extract information about the beam-pipe cross section from the construction drawings. The extracted cross sections can then be treated by fitting the maximum ellipse inscribed into the beam-pipe shape, and this is the shape used in our numerical simulations. Outside the region shown in figure 2, the aperture model has been defined using apertures with nominal cross section.

2024 JINST 19 T06002

2.3 Mechanical model of the internal dump

The internal dumps were already installed in the middle of SS47 and SS48 (the official name is TDI.47 and TDI.48, respectively) [11], and this configuration has been retained even for the new internal dumps developed in the LIU project framework [1, 2]. The new dump design has been developed with the goal of surviving the increase in beam brightness. These dumps are used during beam operation to protect the ring hardware from beam-induced damage or simply to dump the beams at a given time in the magnetic cycle during a set-up phase. In this respect, it is worth mentioning that internal dumps can be triggered manually or automatically, using the standard PS ring control system.

Due to space limitations, the new dump core, shown in figure 3, is made of a $180 \times 40 \times 230\,\mathrm{mm}^3$ (W × H × L) block and weights 12.5 kg, which is not long enough to completely absorb all protons beam in the PS range of working energy. The core is made up of two elements [9]: a 12 cm-long graphite block with a density of $1.83\,\mathrm{g\,cm}^{-3}$; an L-shaped block made up of a copper alloy (CuCr1Zr) with 10.8 cm thick feet with a density of $8.9\,\mathrm{g\,cm}^{-3}$.

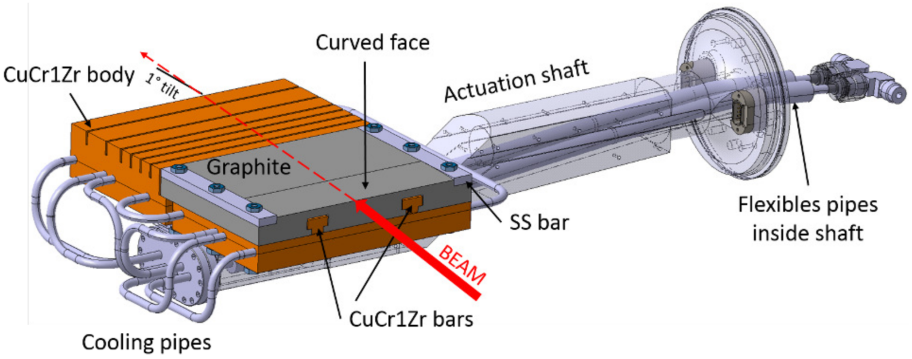

Figure 3. Detail of the design of the dump core design. Reproduced from [9]. CC BY 3.0.

Figure 4 shows a side view of the internal dump in the parking position [9]. The mechanism that controls the movement of the dump is visible. When moving towards the beam, the dump rotates around a pivot point, located at the extremity of the mechanical arm visible in the figure 3. In numerical simulations, the dump moves in the vertical direction with a movement represented by pure translation. The complication of rotational movement has been neglected because the angle of the upper face of the dump core is of the order of 2.6° when the dump touches the beam edge in the extreme case of a large vertical emittance beam. This value decreases to only 0.25° when the upper face of the core crosses the median plane in its centre. These angles generate negligible effects on beams of typical total horizontal beam size $\lesssim 10\,\mathrm{mm}$.

The movement of the new internal dumps is inspired by the design of the previous dump, as it has been proven to be the best suited for the expected performance.

According to the design, the beam interacts first with the graphite part and then with the CuCr1Zr part. A spring is set to vertically move the arm, which rotates around a pivot point, at a speed of 0.8 m/s.[1] This speed is very small compared to the beam speed, and that is why the beam is shaved relatively slowly on a turn-by-turn basis. The duration of the entire beam dump movement was determined based on the operational needs of triggering a dump at the extraction of a cycle

[1]Note that the PS revolution time is approximately 2.1 µs.

2024 JINST 19 T06002

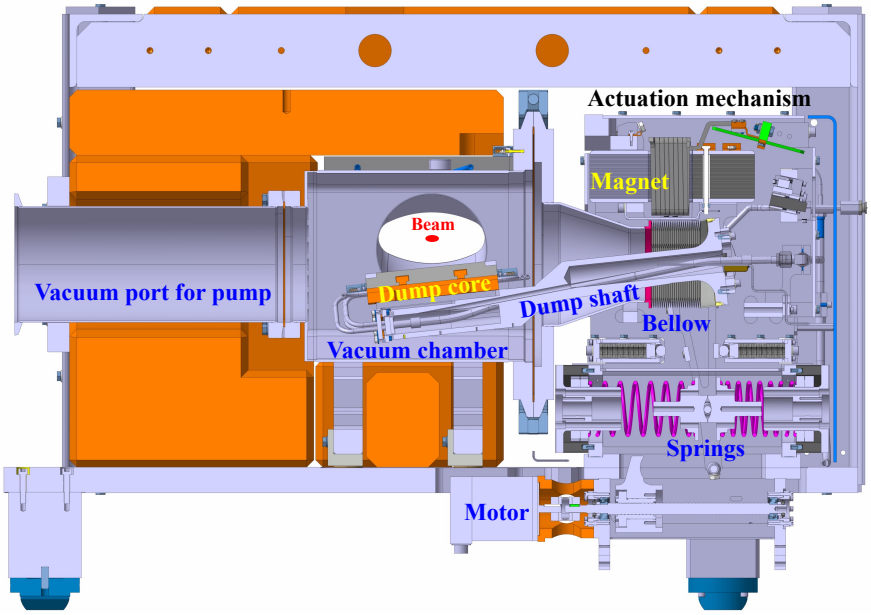

Figure 4. Side view of the internal dump in the parking position. The mechanism that controls the movement of the dump is clearly visible. Reproduced from [9]. CC BY 3.0.

and the same dump is triggered at the injection of the following cycle (corresponding to a delay of approximately 500 ms). The selected actuator mechanism and its speed do not affect the actual shaving time, which typically lasts less than 10 ms and depends on the beam size. During the design phase, the energy deposition maps were divided into time intervals of 150 µs, allowing an accurate estimate of the maximum temperature and stress in the thin shaving layers (a few microns thick) during heat diffusion [7, 8]. For the purposes of this study, the short duration of scraping has negligible impact on the integrated dose distribution along the accelerator's ring, as also suggested by the emittance scans reported in section 3.1.

3 Beam dynamics simulations

3.1 General considerations

The numerical simulations are managed, performed, and analysed by four codes. At the top level, a `Python` script generates the beam distribution, manages the simulation parameters and input files, controls the other codes, and finally analyses the results of the numerical simulations. The beam distribution has been generated in the 6D phase space, using Gaussian functions for the transverse degrees of freedom, whose rms values are given by the beam emittances reported in table 1, and Gaussian functions for the relative momentum spread and bunch length, whose rms values are also given in table 1. `MAD-X` combined with `PTC` [21] is used to generate the appropriate lattice configuration, Twiss tables, and input files for `SixTrack` [22]. `SixTrack` performs initial condition tracking and simulates the interaction between the beam and the internal dump using an active coupling with `FLUKA` [5, 6, 23, 24]. Finally, special `FLUKA` output files are used for the shower simulations presented and discussed in section 4 and compared with beam-based measurements. Each simulation consists of

2024 JINST 19 T06002

a total of 10^6 initial conditions (distributed according to the beam parameters listed in table 1) that are tracked around the ring until they are all lost in the internal dump or in the mechanical aperture. The start of beam simulations corresponds to the internal dump set at a position of -10σ, then moving at constant speed until all particles are lost and, with the number of initial conditions considered in our studies, no beam losses are observed until the dump is at -6σ.

The sensitivity of beam losses during the dump process to the value of the transverse beam emittances has been probed in detail. Scans of ±40 % around the values of the horizontal and vertical emittances reported in table 1 have been carried out. The corresponding changes in the observed beam loss in the mechanical aperture are tiny, at a level of approximately 0.01 %, and therefore completely negligible.

The impact of synchrotron motion has been carefully assessed and found to be negligible, at the level of numerical accuracy, due to the statistic of the set of initial conditions. For this reason, the numerical simulations reported here have been performed without synchrotron motion, using initial beam distributions generated in the 4D transverse phase space.

3.2 Ring losses due to internal dump activation

The results of the numerical simulations are shown in figure 5 where the distribution of beam losses along the PS ring circumference are shown for the LHC FT case when the TDI.47 (top) or the TDI.48 (bottom) are activated. Note that initially, the closed orbit distortion computed from the beam measurements has not been included (see section 3.3 for the evaluation of the impact of the closed orbit distortion). These distributions are obtained from the results of numerical simulations, in which an initial condition crossing the mechanical aperture is counted as lost, by introducing a binning of the variable s with a width of 10 cm. The time dependence of the beam losses is encoded in the colour scale. The first observation is that the losses are concentrated in a region of the circumference of the PS of approximately 80 m to 100 m downstream of the internal dump. The rest of the circumference of the ring does not suffer from beam losses during the activation of the dumps. The beam losses start in the close vicinity of the dump and then propagate towards the end of the region.

It takes approximately 3×10^3 turns or 4×10^3 turns to dump the entire beam when TDI.47 or TDI.48 is activated, respectively. This is due to the difference in beam size at the location of the two internal dumps. The PS lattice features maximum horizontal and minimum vertical beta functions in odd straight sections and the opposite in even straight sections, and we have $\beta_{\mathrm{V,SS47}} \approx 11$ m ($\beta_{\mathrm{H,SS47}} \approx 22$ m, $D_{\mathrm{H,SS47}} \approx 3$ m), while $\beta_{\mathrm{V,SS48}} \approx 22$ m ($\beta_{\mathrm{H,SS48}} \approx 11$ m, $D_{\mathrm{H,SS47}} \approx 2$ m).

A direct comparison of the total beam losses generated by the two dumps is shown in figure 6. Qualitatively, the distributions are very similar, in particular for the case of the losses observed in the same straight section where the dump is installed. Downstream, the detailed evolution of the beam losses is different, although the integral of the losses in each straight section is globally rather similar. Note that TDI.47 generates losses that cover a larger extent of the circumference of the PS ring. On the other hand, as seen in tables 2 and 3, the total amount of beam losses generated by the use of dumps is very similar. Therefore, in the case of TDI.47, the losses spread over a larger region of the PS ring, implying lower local levels of radiation dose compared to those generated by the use of TDI.48. However, a larger part of the ring will be affected by these losses, which could pose problems in terms of hands-on maintenance of the hardware installed there.

2024 JINST 19 T06002

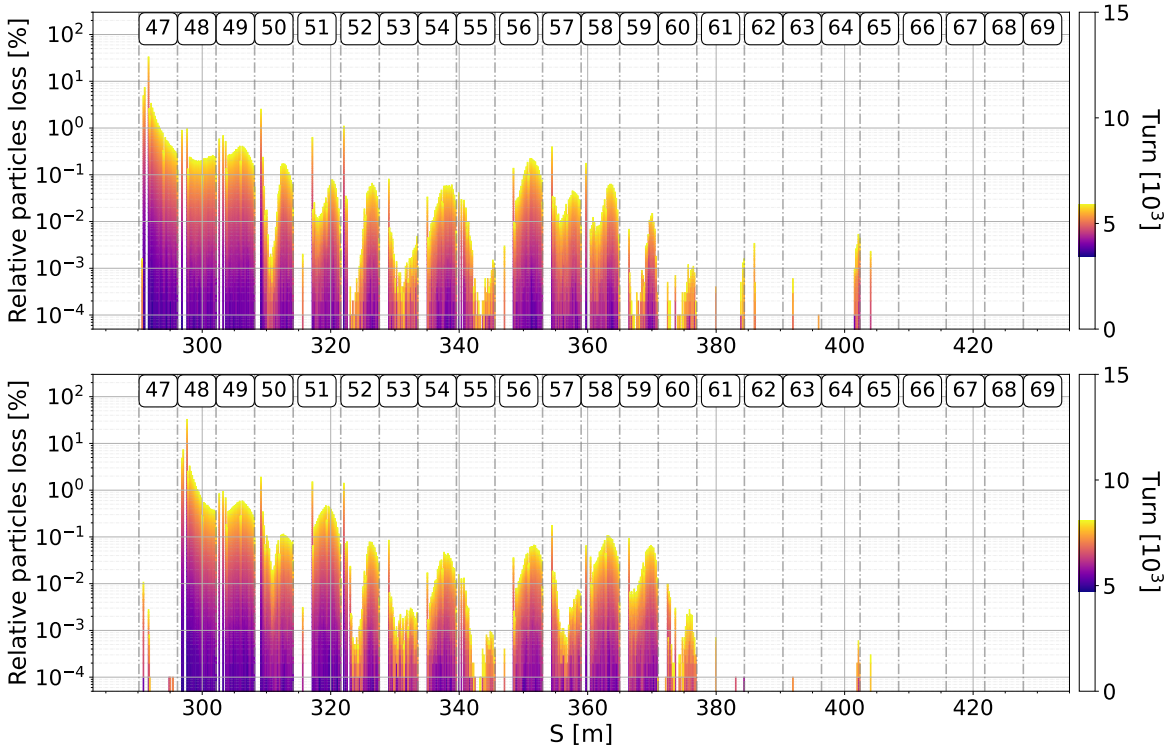

Figure 5. Distribution of beam losses on the mechanical aperture along the PS ring circumference for the case LHC FT when the TDI.47 (top) and TDI.48 (bottom) are activated. The colour scale encodes the time evolution of the beam losses (the white regions represent the time intervals during which no beam losses occur).

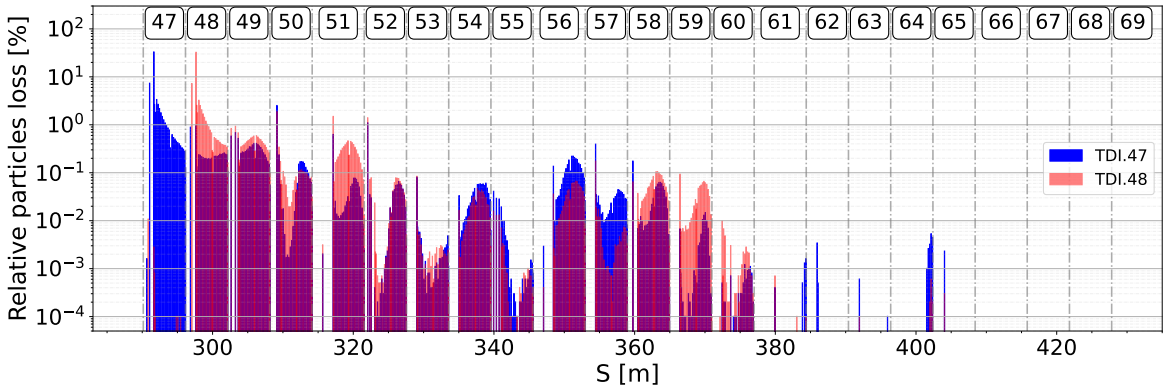

Figure 6. Difference in distribution of beam losses on the mechanical aperture along the circumference of the PS ring for the case LHC FT when the two internal dumps are activated.

The dependence of beam losses on beam energy is shown in figure 7. The extent of the region in which the beam losses are distributed is essentially independent of the beam energy. In terms of the time dependence of the beam losses, the time to dump the entire beam is approximately 3×10^3, 6×10^3, and 7×10^3 turns for 26, 14, and 3.9 GeV/c, respectively, for TDI.47.

A quantitative comparison of losses for the three configurations under consideration can be made by considering the fraction of initial conditions lost in the mechanical aperture or in the dump

2024 JINST 19 T06002

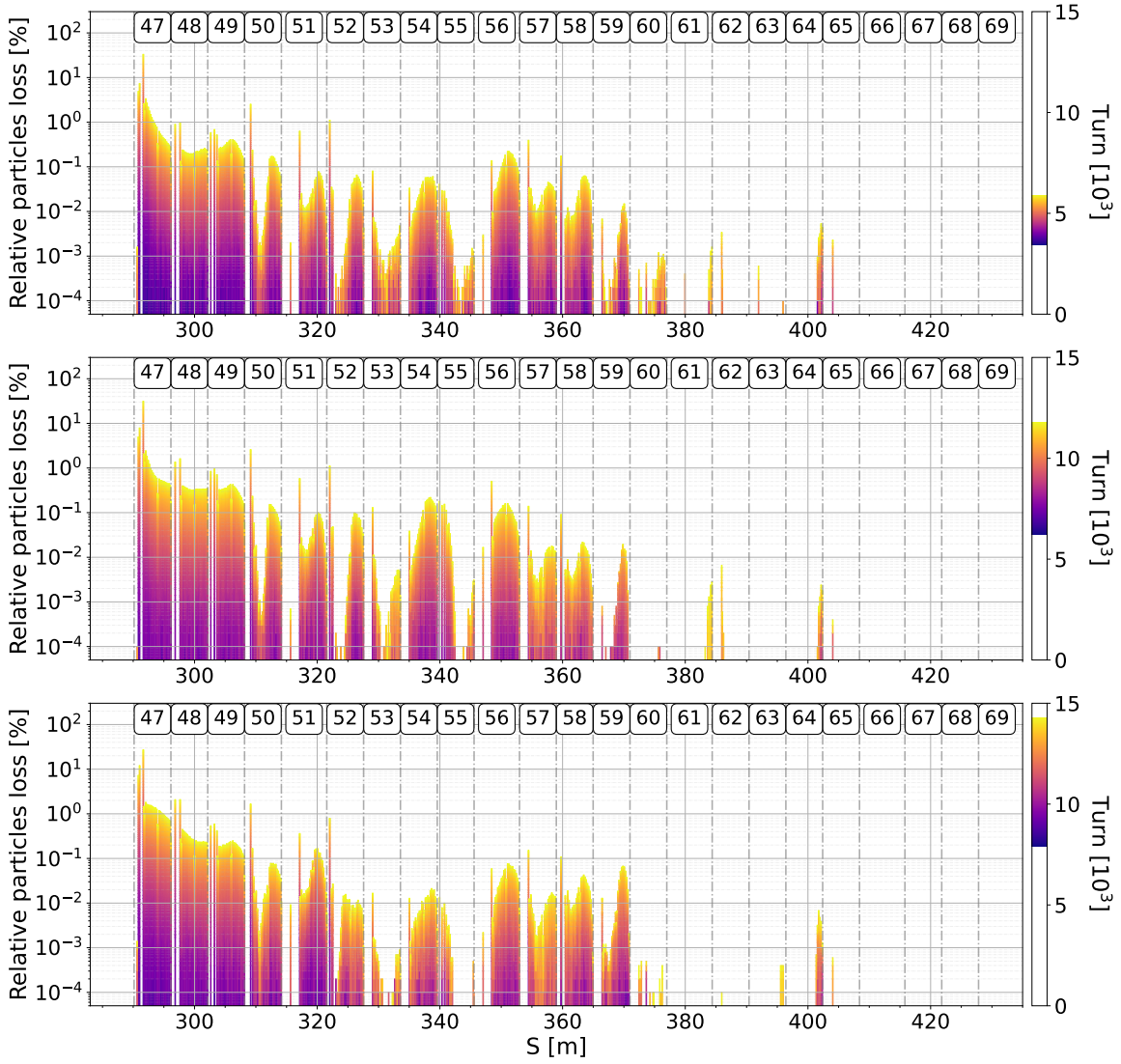

Figure 7. Distribution of beam losses on the mechanical aperture along the PS ring circumference for the case LHC FT (top), SFTPRO FT (middle), and LHC FI (bottom) when the TDI.47 is activated. The colour scale encodes the time evolution of the beam losses (the white regions in the bar represent the time intervals during which no beam losses occur).

and this account is reported in table 2. The numbers quoted do not depend much on the dump considered, whereas they show a certain dependence on the beam energy. Losses in the mechanical aperture decrease with decreasing beam energy, whereas the opposite occurs for the fraction of protons absorbed by the dump. The large interval of transverse emittances probed in exploratory numerical simulations did not show a dependence of the beam losses on the value of the transverse emittances, as mentioned above. Therefore, the energy dependence of the beam losses summarised in tables 2 and 3 is due to the dependence of the beam-dump interaction.

As a general observation, the striking feature of these studies is the large amount of beam loss in the mechanical aperture with respect to the beam absorbed by the dump, which corresponds to a dump behaviour much like that of a beam spreader rather than a beam stopper.

2024 JINST 19 T06002

Table 2. Fraction of beam losses in the dump and in the mechanical aperture for both internal dumps and the three beam types. The beam losses in the dump represent primary protons that have undergone nuclear interaction, while for the rest of the ring, they represent impacts on the aperture.

	TDI.47			TDI.48		
	LHC FT	**SFTPRO FT**	**LHC FI**	**LHC FT**	**SFTPRO FT**	**LHC FI**
P [GeV/c]	26	14	3.9	26	14	3.9
Dump [%]	4.9	5.0	7.3	4.8	4.9	7.2
Aperture [%]	95.1	95.0	92.7	95.2	95.1	92.8

3.3 Effect of the closed orbit distortion on the distribution of beam losses

The impact of the closed-orbit distortion has been scrutinised in detail. Figure 8 compares the loss distribution with and without closed-orbit distortion. The observed discrepancies are below the percent level. Stronger effects are observed for LHC FT, which is in agreement with the observation of a larger closed-orbit distortion in that case. For the SFTPRO FT and LHC FI cases, the presence of closed-orbit distortion has a mild impact on the results of numerical simulations, once again in qualitative agreement with the behaviour of the closed orbit measurements.

Table 3 presents the updated fraction of particles that were lost in the dump and in the aperture for the various configurations when the closed-orbit distortion is included in the numerical simulations. The reported values remain fairly close to the estimate without a closed orbit in table 2. In general, there are approximately 0.4 % more primary particles hitting the aperture when considering the closed orbit.

Table 3. Fraction of beam losses in the dump and in the mechanical aperture for both internal dumps and the three beam types when the closed-orbit distortion is included in the numerical simulations.

	TDI.47			TDI.48
	LHC FT	**SFTPRO FT**	**LHC FI**	**LHC FT**
P [GeV/c]	26	14	3.9	26
Dump [%]	4.5	4.6	6.1	4.4
Aperture [%]	95.5	95.4	93.9	95.6

4 Shower simulations and comparison with beam-based measurements

4.1 Framework of the simulations

Based on the results of the numerical simulations presented above, we can determine the position, direction, and energy of primary protons when they strike the internal dump on each turn around the ring. The identified particle distribution with closed-orbit distortion is introduced as a source term in a `FLUKA` simulation, taking into account the position of the internal dump at each turn, so that each proton interacting with it is scattered off or creates a particle shower. The simulation determines the development of this shower and its interactions with all beam elements present in the

2024 JINST 19 T06002

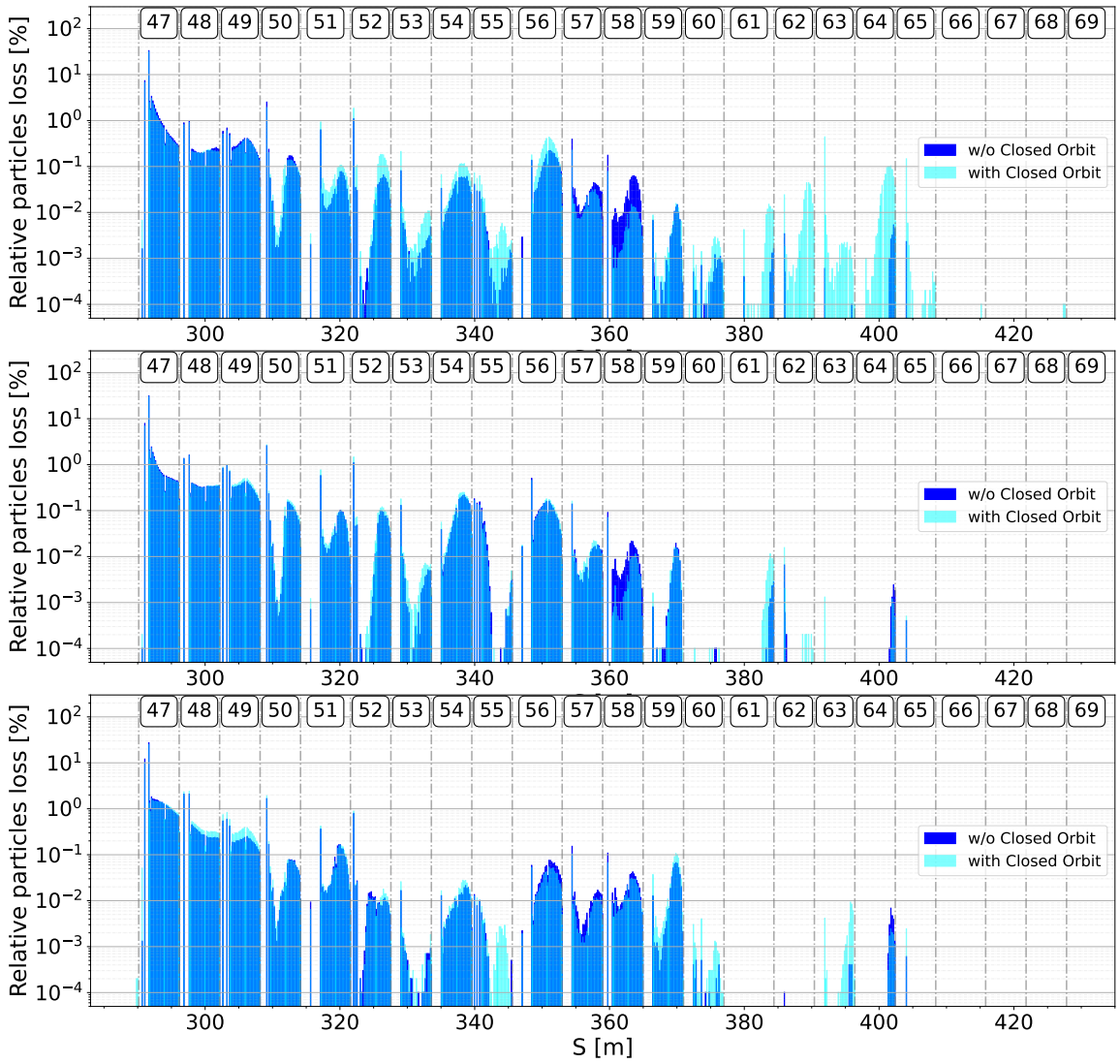

Figure 8. Effect of the closed-orbit distortion on the distribution of beam losses for LHC FT (top), SFTPRO FT (middle), and LHC FI (bottom) when the TDI.47 is activated.

ring lattice, from SS47 to SS69 (representing a region 150 m long). Magnetic fields are implemented inside the vacuum pipes of the main magnet units. To reproduce the effect of magnetic errors that generate the closed-orbit distortion (as shown in figure 1) for scattered protons as well, the virtual orbit correctors were included in the FLUKA model. Figure 9 shows a 3D visualisation of the geometry model implemented in the FLUKA simulations.

As mentioned in section 2, the dump speed is approximately 0.8 m s^{-1}, hence the beam is fully stopped after about a few thousand turns, which corresponds to approximately a few ms in duration.

The scenarios used in the FLUKA simulations are the same as those described in table 1. In the case of the study of the dump TDI.47, all these scenarios are used, while for the case of TDI.48 we have limited our considerations to the LHC FT case.

To validate our FLUKA simulations, our objective was to compare the numerical results with those of the beam measurements. This comparison is carried out by looking at the doses recorded by the

2024 JINST 19 T06002

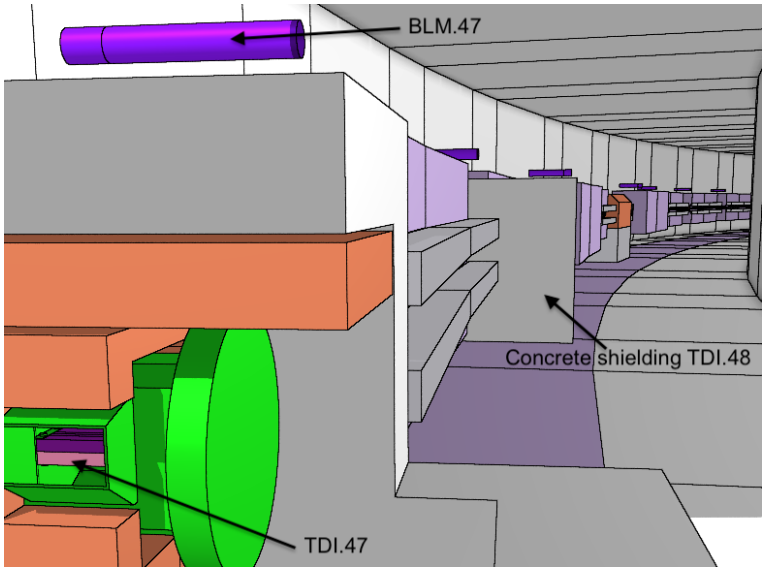

Figure 9. 3D visualisation of the FLUKA model using FLAIR [25].

BLM installed on the main magnets of the PS ring [26]. During dedicated experimental studies, the dumps were intentionally activated at various beam intensities with the aim of determining the dose recorded by each BLM per primary particle of the stopped beam.

Figure 10 illustrates the time evolution of key parameters, such as beam intensity, beam momentum, and dose in BLM.47 over a typical PS LHC beam production cycle. When the exact moment of dump activation is determined, it becomes possible to accurately determine the dose recorded by each BLM.

In our analysis, the statistical uncertainty is estimated based on 5 to 10 measurements performed across different beam intensities. Furthermore, the systematic uncertainty, influenced by the response of the BLMs and the beam current transformer, is considered below 1 %.

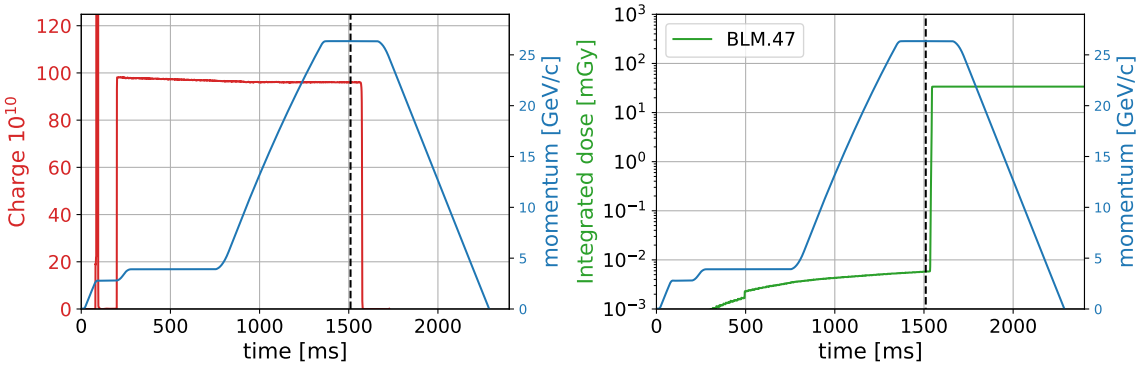

Figure 10. The blue curves show the momentum evolution throughout a typical PS LHC beam production cycle. The red curve represents the beam intensity evolution (left). The green curve represents the cumulative dose recorded by BLM.47 (right). Vertical dashed black lines indicate the time when the TDI.47 is activated.

As shown in figure 10, we determine the beam intensity absorbed by the dump based on the charge measurement taken just before the dump is activated. The total dose is calculated by accumulating the dose readings from the BLMs, carefully excluding any losses that occurred before the dump

2024 JINST 19 T06002

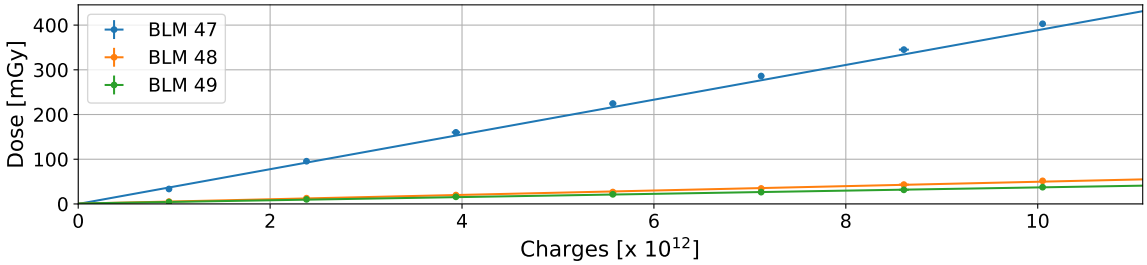

Figure 11. Dose recorded in the three first BLMs for the LHC FT case when the dump TDI.47 is activated. A linear relationship is clearly visible.

activation. As expected, a linear relationship is evident between the beam intensity and the detector response, as depicted in figure 11.

4.2 Comparison between FLUKA simulations and measured beam data

Figures 12 and 13 show the comparison between the measured and simulated dose data.

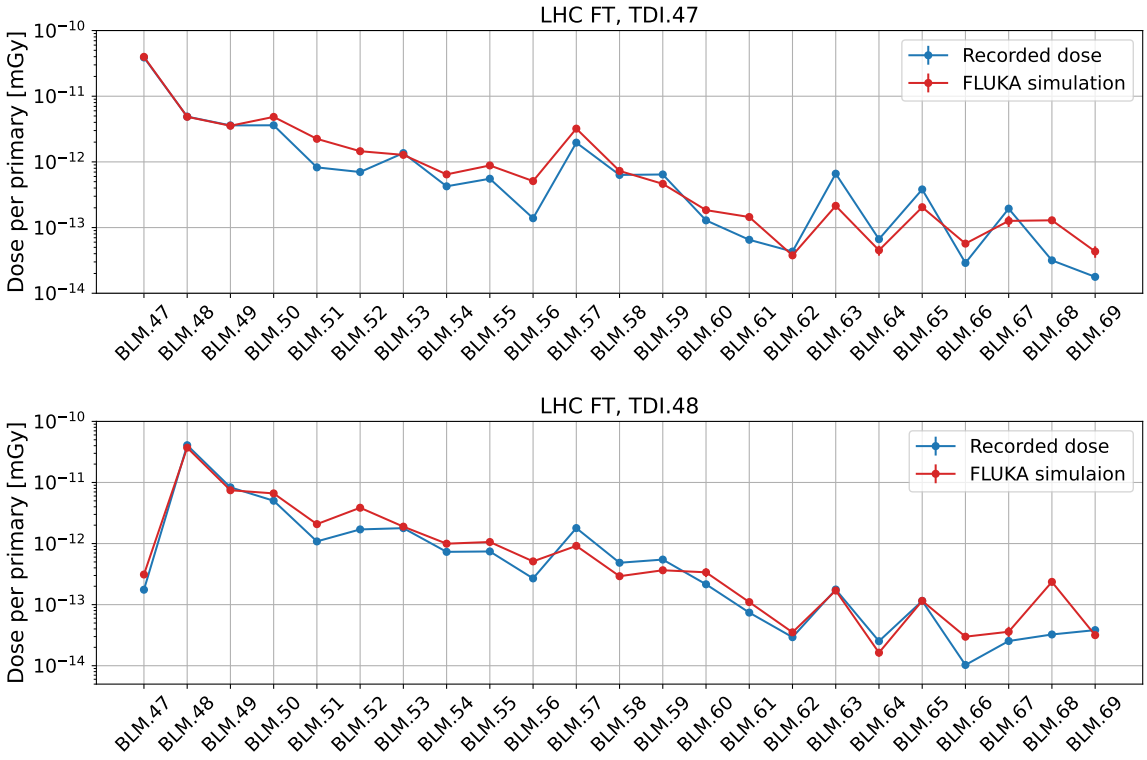

Figure 12. Loss maps measured by means of the BLMs (blue) and computed from the FLUKA simulations (red) in the LHC FT case when the dump TDI.47 (top) or TDI.48 (bottom) are activated.

When examining the results of the LHC FT case, as illustrated in figures 12 and 13 (top), it becomes evident that, while there is satisfactory agreement between the beam data and the simulation predictions, certain discrepancies can be observed. A plausible explanation for these differences could be attributed to some of the simplifications implemented in the aperture model and to the fact that

2024 JINST 19 T06002

magnetic fields are implemented only inside the vacuum pipes of the main magnet units. It should be noted, for example, that some components, such as beam wire scanners (in SS54, 64, 65, 68) or RF cavities (in SS51, 56, and 66), are not included in the FLUKA aperture model.

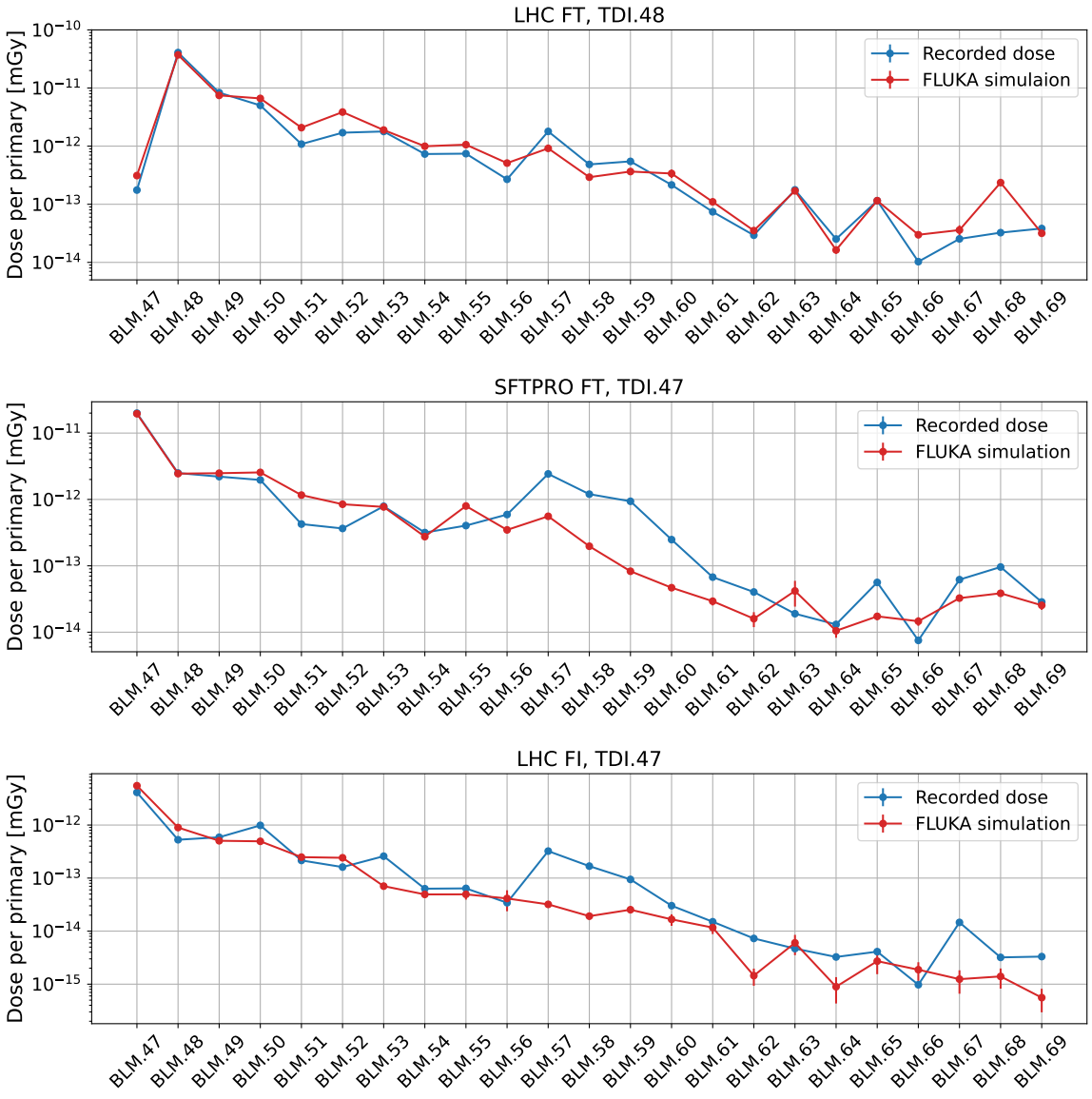

Figure 13. Loss maps measured by the BLMs (blue) and computed from the FLUKA simulations (red) in the LHC FT (top), SFTPRO FT (middle), and LHC FI (bottom) cases when the dump TDI.47 is activated.

At lower energies, as shown in figure 13 (middle, bottom), a notable discrepancy is observed between SS57 and SS61. Furthermore, this discrepancy continues until the end of the considered ring region even at lower energies. Efforts were devoted to determining sources for the observed discrepancies other than the aperture model. In fact, the BLMs are mounted on rails and are fixed on top of the PS main magnets. However, an error margin of ±5 cm is allowed in the transverse direction. To rule out the potential misplacement of the BLMs as a source of the observed discrepancies, simulations with added offsets were performed. The results are depicted in figure 14. It is evident

2024 JINST 19 T06002

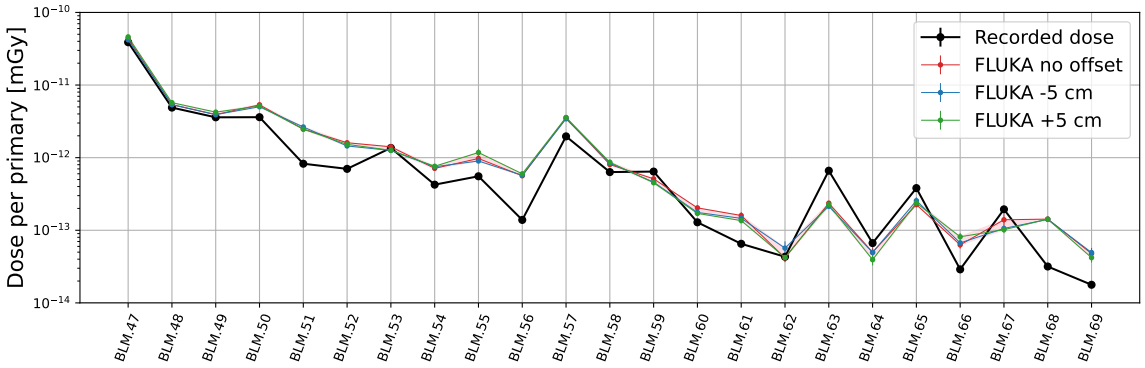

Figure 14. Loss maps measured by the BLMs (black) and computed from the FLUKA simulation in the LHC FT case when the dump TDI.47 is activated. Some curves have been generated by introducing position offsets along the transverse horizontal coordinate.

from this plot that although an offset could alter the dose values recorded by BLMs, these variations are not sufficient to account for the discrepancies noted above.

All in all, despite some discrepancies, it is worth stressing that there is generally good agreement in the patterns across almost four orders of magnitude. This consistency suggests that our model is predictive and capable of making accurate predictions.

4.3 Absorbed dose in the elements of the PS ring

To estimate the annual dose absorbed by various accelerator components, certain conservative assumptions were made. Specifically, according to the specifications in ref. [18], it is assumed that 5×10^{13} protons are directed to the TDI.47 dump at maximum energy, i.e., P = 26 GeV/c, in a single cycle.

Figure 15 depicts the energy density absorbed by TDI.47 when subjected to an LHC beam at flat top. For each pulse, the energy deposited into the dump is approximately 11 kJ, representing 5.7% of the total kinetic energy of the beam. These results align with those reported in ref. [9].

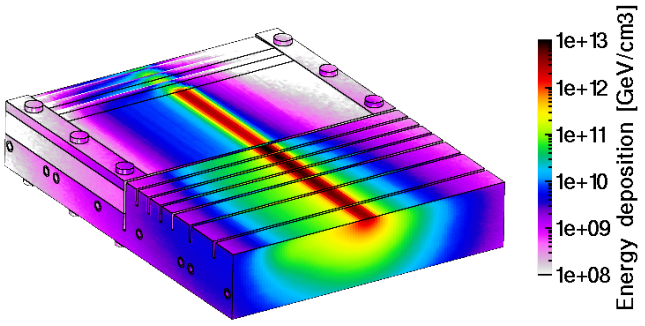

Figure 15. Energy density in the TDI.47 when it is activated in the LHC FT case normalised to an intensity of 5×10^{13} protons.

Table 4 provides detailed information on where the remaining energy is absorbed. It can be seen that almost half of the total kinetic energy of the beam is absorbed by the main magnets, while the

2024 JINST 19 T06002

tank and the shielding surrounding the internal dump absorb 13.1 % of the energy. A fraction of the beam energy is converted into neutrinos (1.5 % of the energy), while another fraction is converted to mass in nuclear reactions (8.5 % of the energy). Furthermore, 0.7 % of the energy escapes the boundary of the region assumed in the FLUKA simulation.

Table 4. Breakdown of the absorbed fraction of the beam kinetic energy in the different equipment and in the tunnel wall for the LHC FT case when the TDI.47 is activated.

Absorption elements	**% of beam kinetic energy**
Main magnets	49.0
Tank/shielding TDI.47	13.1
Tunnel wall	11.4
TDI.47	5.7
Tank/shielding TDI.48	4.5
Other elements	3.2
Beam pipes	2.3
Air	0.1
Nuclear reactions	8.5
Neutrinos	1.5
Outside geometry boundaries	0.7

Figure 16 shows the annual dose accumulated in both the main magnets and the BLMs. Following the assumptions outlined in ref. [18], it is assumed that the dump stops 2.4×10^{17} protons for a typical PS run spanning one year. For a conservative approach, we considered that all protons stop under conditions similar to those in the LHC FT case.

The main magnet just downstream of the dump and the focusing unit of the main magnet in two straight sections further downstream are the devices subject to the highest dose levels. They absorb a dose that is at least an order of magnitude higher than that in the magnets further downstream. Additionally, the dose absorbed by the magnet coils is significantly greater than that absorbed by the yoke, highlighting the possibility of localised energy-deposition hot spots.

The maximum dose received in the first coil, as illustrated in figure 16, is 0.36 MGy per year. The most restrictive element in terms of dose received is coil insulation, which, in our case, is based on epoxy, which can tolerate up to 10 MGy [27]. This seems to indicate that the current values are not alarming. However, additional studies are warranted to ensure a complete understanding of the situation.

5 Conclusions

This paper reports the results of several simulation studies considering the interaction of protons beam at different energies on a moving internal dumps in the PS ring. The detailed analyses presented here are devoted to understanding how the particles are scattered downstream of those dumps. Two types of study have been presented, namely simulations of the beam dynamics combined with the beam-dump interaction and simulations of the particle showers induced by the beam interaction with the internal dump.

2024 JINST 19 T06002

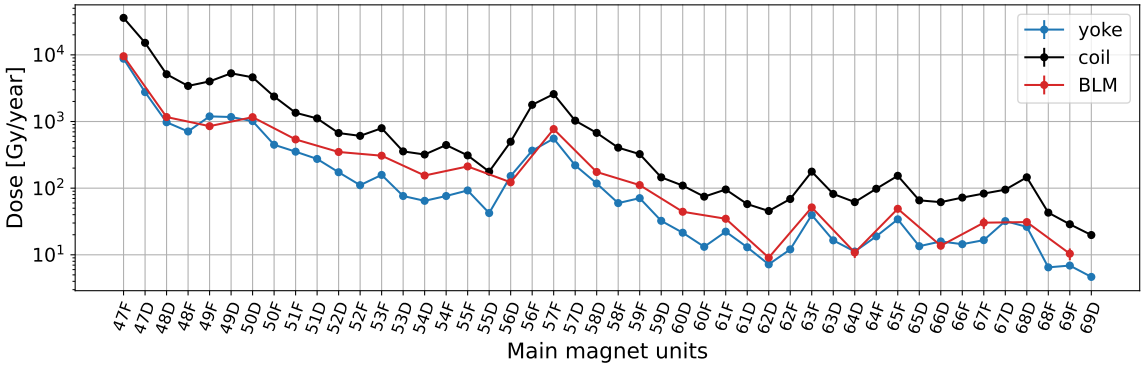

Figure 16. Total integrated dose in the yoke and coils of the PS main magnets accumulated after a year of regular operation (assuming 2.4×10^{17} protons are stopped in the dump in one year) for LHC FT case when the TDI.47 is used. The absorbed dose in the BLMs is also shown. The F and D letters refer to the focusing and defocusing half-unit of each magnet, respectively.

The goal of the first type of simulation has been to develop an accurate model of the beam dynamics at various beam energies. The accuracy of the model has been improved by introducing the non-negligible closed-orbit distortion measured in the PS ring. The main result of these analyses is that the beam losses cover a limited region of the PS ring circumference, and the features of the loss distribution are rather stable, regardless of the internal beam dump used. Furthermore, a limited fraction of the beam intensity is deposited in the beam dump, which acts as a scatterer rather than a real dump.

Simulations of particle showers confirmed that the accuracy of the model allows us to predict the dose distribution across various sections of the accelerator, which is in good agreement with the beam measurements performed with the BLM system. The aperture model used in these simulations should be improved, as observed in the analyses made. Simulations revealed that, at maximum energy, the dumps absorb approximately 6% of the beam energy. Most of the residual energy is dissipated by the components of the ring and the adjacent walls.

Future studies will focus on determining more accurate estimates of the typical number of protons stopped and their energy in a yearly run, based on the actual use of the internal dump. This analysis may lead to recommendations on the need to improve the shielding around the dumps.

Acknowledgments

We would like to thank R. De Maria and F.F. Van der Veken for his help and support with the numerical simulations of beam dynamics with `SixTrack` and the coupling with `FLUKA`. We would like to express our gratitude to François-Xavier Nuiry for several discussions on the mechanical design of the new internal targets.

This article is an updated version of the HB 2023 conference proceeding, published under CC BY 3.0 license as [28, 29].

References

[1] H. Damerau et al., *LHC Injectors Upgrade, Technical Design Report: Volume 1: Protons*, CERN-ACC-2014-0337 CERN, Geneva, Switzerland (2014) [DOI:10.17181/CERN.7NHR.6HGC].

2024 JINST 19 T06002

[2] *LHC Injector Upgrade Project*, https://espace.cern.ch/liu-project/default.aspx.

[3] G. Apollinari et al., *High-Luminosity Large Hadron Collider (HL-LHC): Technical Design Report V. 0.1*, CERN-2017-007-M, vol. 4 of *CERN Yellow Rep. Monogr.*, CERN, Geneva, Switzerland (2017) [DOI:10.23731/CYRM-2017-004].

[4] *FLUKA*, https://fluka.cern/.

[5] C. Ahdida et al., *New Capabilities of the FLUKA Multi-Purpose Code*, *Front. Phys.* **9** (2022) 788253.

[6] G. Battistoni et al., *Overview of the FLUKA code*, *Annals Nucl. Energy* **82** (2015) 10.

[7] J. Briz Monago et al., *Multi-turn Study in FLUKA for the Design of CERN-PS Internal Beam Dumps*, in the proceedings of the *9th International Particle Accelerator Conference*, Vancouver, Canada, 29 April–4 May 2018, pp. 724–727 [DOI:10.18429/JACoW-IPAC2018-TUPAF025].

[8] G. Romagnoli et al., *Design of the New PS Internal Dumps, in the Framework of the LHC Injector Upgrade (LIU) Project*, in the proceedings of the *8th International Particle Accelerator Conference*, Copenhagen, Denmark, 14–19 May 2017, pp. 3521–3523 [DOI:10.18429/JACoW-IPAC2017-WEPVA109].

[9] G. Romagnoli et al., *Engineering Design and Prototyping of the New LIU PS Internal Beam Dumps*, in the proceedings of the *9th International Particle Accelerator Conference*, Vancouver, Canada, 29 April–4 May 2018, pp. 2600–2603 [DOI:10.18429/JACoW-IPAC2018-WEPMG001].

[10] J. Barranco Garcia and S. Gilardoni, *Simulation and optimization of beam losses during continuous transfer extraction at the CERN Proton Synchrotron*, *Phys. Rev. ST Accel. Beams* **14** (2011) 030101.

[11] S. Gilardoni and D. Manglunki, *Fifty years of the CERN Proton Synchrotron: Volume 1*, *CERN Yellow Rep. Monogr.* (2011) [DOI:10.5170/CERN-2011-004].

[12] PS Multi-Turn Extraction Study Group, *The CERN PS multi-turn extraction based on beam splitting in stable islands of transverse phase space: Design report*, CERN-2006-011 *CERN Yellow Rep. Monogr.* (2006) [DOI:10.5170/CERN-2006-011].

[13] E. Regenstreif, *The CERN proton synchrotron (1st Part)*, CERN-59-29, *CERN Yellow Rep. Monogr.*, CERN, Geneva, Switzerland (1959) [DOI:10.5170/CERN-1959-029].

[14] E. Regenstreif, *The CERN Proton Synchrotron (2nd Part)*, CERN-60-26, *CERN Yellow Rep. Monogr.*, CERN, Geneva, Switzerland (1960) [DOI:10.5170/CERN-1960-026].

[15] E. Regenstreif, *The CERN proton synchrotron (3rd Part)*, CERN-62-03, *CERN Yellow Rep. Monogr.*, CERN, Geneva, Switzerland (1962) [DOI:10.5170/CERN-1962-003].

[16] E. Regenstreif, *The CERN proton synchrotron, 1*, *Ned. T. Natuurk.* **25** (1959) 117.

[17] E. Regenstreif, *The CERN proton synchrotron, 2*, *Ned. T. Natuurk.* **25** (1959) 149.

[18] F.-X. Nuiry and G. Romagnoli, *PS Ring Internal Dumps Functional Specifications*, EDMS 1582110, PS-TDI-ES-0001, CERN, Geneva (2017).

[19] R. Steerenberg and D. Cotte, *PS Beam Spot Sizes for the Design of New Internal Beam Dumps*, EDMS 1612293, CERN, Geneva (2017), https://edms.cern.ch/ui/file/1612293/1/PS_Beam_Size_Calculations_InternalDumps.pdf.

[20] *MAD — Methodical Accelerator Design*, https://mad.web.cern.ch/mad/.

[21] E. Forest, Y. Nogiwa and F. Schmidt, *The FPP and PTC Libraries*, in the proceedings of the *9th International Computational Accelerator Physics Conference*, Chamonix, France, 2–6 October 2006, pp. 17–21, https://jacow.org/icap06/papers/MOM1MP02.pdf.

2024 JINST 19 T06002

[22] R. De Maria et al., *SixTrack Version 5: Status and new developments*, in the proceedings of the *10th International Particle Accelerator Conference*, Melbourne, Australia, 19-24 May 2019, pp. 3200–3203 [DOI:10.18429/JACoW-IPAC2019-WEPTS043].

[23] A. Mereghetti et al., *SixTrack-Fluka Active Coupling for the Upgrade of the SPS Scrapers*, in the proceedings of the *4th International Particle Accelerator Conference*, Shanghai, China, 12–17 May 2013, pp. 2657–2659.

[24] S. Redaelli, ed., *ICFA Mini-Workshop on Tracking for Collimation in Particle Accelerators: CERN, Geneva, Switzerland, 30 October 2015*, *CERN Yellow Rep. Conf. Proc.* CERN, Geneva (2018) [DOI:10.23732/CYRCP-2018-002].

[25] V. Vlachoudis, *Flair: A powerful but user friendly graphical interface for FLUKA*, in the proceedings of the *International Conference on Mathematics, Computational Methods & Reactor Physics*, Saragota Springs, NY, U.S.A., 3–7 May 2009, pp. 790–800.

[26] E. Effinger et al., *Beam Loss Monitors Comparison at the CERN Proton Synchrotron*, *Conf. Proc. C* **110904** (2011) 1341.

[27] P. Beynel, P. Maier and H. Schonbacher, *Compilation of radiation damage test data. Part III. Materials used around high-energy accelerators*, CERN-82-10, *CERN Yellow Rep. Monogr.*, CERN, Geneva, Switzerland (1982) [DOI:10.5170/CERN-1982-010].

[28] S. Niang et al., *Shower Simulations for the CERN Proton Synchrotron Internal Dump and Comparison with Beam Loss Monitor Data*, in the proceedings of the *68th ICFA Advanced Beam Dynamics Workshop on High-Intensity and High-Brightness Hadron Beams — HB2023*, CERN, Geneva, Switzerland, 9–13 October 2023, pp. 389–392 [DOI:10.18429/JACoW-HB2023-THC2C1].

[29] T. Pugnat et al., *Study of the Performance of the CERN Proton Synchrotron Internal Dump*, in the proceedings of the *68th ICFA Advanced Beam Dynamics Workshop on High-Intensity and High-Brightness Hadron Beams — HB2023*, CERN, Geneva, Switzerland, 9–13 October 2023, pp. 555–558 [DOI:10.18429/JACoW-HB2023-THBP36].

2024 JINST 19 T06002